

Cross-Correlating the Universe: The Gravitational Wave Background and Large-Scale Structure

Federico Semenzato ^{*}

*Dipartimento di Fisica Galileo Galilei, Università di Padova, I-35131 Padova, Italy and
INFN Sezione di Padova, I-35131 Padova, Italy*

J. Andrew Casey-Clyde

*Department of Physics, University of Connecticut, 96 Auditorium Road, U-3046, Storrs, CT 06269-3046, USA and
Department of Physics, Yale University, New Haven, CT, 06520, USA*

Chiara M. F. Mingarelli[†]

Department of Physics, Yale University, New Haven, CT, 06520, USA

Alvise Raccanelli,[‡] Nicola Bellomo,[§] Nicola Bartolo, and Daniele Bertacca
*Dipartimento di Fisica Galileo Galilei, Università di Padova, I-35131 Padova, Italy
INFN Sezione di Padova, I-35131 Padova, Italy and
INAF-Osservatorio Astronomico di Padova, Italy*

The nature of the gravitational wave background (GWB) is a key question in modern astrophysics and cosmology, with significant implications for understanding of the structure and evolution of the Universe. We demonstrate how cross-correlating large-scale structure (LSS) tracers with the GWB spatial anisotropies can extract a clear astrophysical imprint from the GWB signal. Focusing on the unresolved population of supermassive black hole binaries (SMBHBs) as the primary source for the GWB at nanohertz frequencies, we construct full-sky maps of galaxy distributions and characteristic strain of the GWB to explore the relationship between GWB anisotropies and the LSS. We find that at current pulsar timing array (PTA) sensitivities, very few loud SMBHBs act as Poisson-like noise. This results in anisotropies dominated by a small number of sources, making GWB maps where SMBHBs trace the LSS indistinguishable from a GWBs from a uniform distribution of SMBHBs. In contrast, we find that the bulk of the unresolved SMBHBs produce anisotropies which mirror the spatial distribution of galaxies, and thus trace the LSS. Importantly, we show that cross-correlations are required to retrieve a clear LSS imprint in the GWB. Specifically, we find this LSS signature can be measured at a 3σ level in near-future PTA experiments that probe angular scales of $\ell_{\max} \geq 42$, and 5σ for $\ell_{\max} \geq 72$. Our approach opens new avenues to employ the GWB as an LSS tracer, providing unique insights into SMBHB population models and the nature of the GWB itself. Our results motivate further exploration of potential synergies between next-generation PTA experiments and cosmological tracers of the LSS.

I. INTRODUCTION

All Pulsar timing array (PTA) experiments have now reported evidence for a gravitational wave background (GWB) [1–4] at nanoHertz frequencies. The primary source of the GWB is likely the superposition of low-frequency GWs from the cosmic merger history of supermassive black hole binaries (SMBHBs; [5–8]), though there may be contributions from cosmological sources [9–13]. In fact, the very large amplitude of the GWB raises important questions about its origin, and this is under active investigation, see e.g. [14].

As PTA experiments mature, add pulsars and improve instrumentation, we will be able to fully characterize the GWB. This characterization includes GWB

map-making [15, 16], and more precisely measuring the GWB’s amplitude and strain spectrum [1, 2, 8]. These measurements will provide more clues as to the composition of the GWB, and the physics sourcing it: a GWB sourced by SMBHBs will show signs of discreteness in the characteristic strain spectrum in the form of excursions from the $h_c(f) \propto f^{-2/3}$ power-law [17], due to a relative over-or-under-density of SMBHBs at a specific frequency, while a cosmological background will be smooth.

These binaries are hosted at the center of massive galaxies which result from galaxy major mergers [18, 19], and thus trace the history of galaxy evolution. Therefore the spatial distribution of SMBHBs is expected to be correlated to that of galaxies, see Figure 1. A GWB generated by SMBHBs hence inherits the spatial distribution of their host galaxies. This opens the possibility of exploiting GWB anisotropies to probe the LSS, as these anisotropies act as a novel tracer of the underlying dark matter distribution – so-called *cosmic web*. While all GWB anisotropies can be traced back to the LSS, nearby SMBHBs can introduce strong anisotropies that

^{*} federico.semenzato.1@phd.unipd.it

[†] chiara.mingarelli@yale.edu

[‡] alvise.raccanelli.1@unipd.it

[§] nicola.bellomo@unipd.it

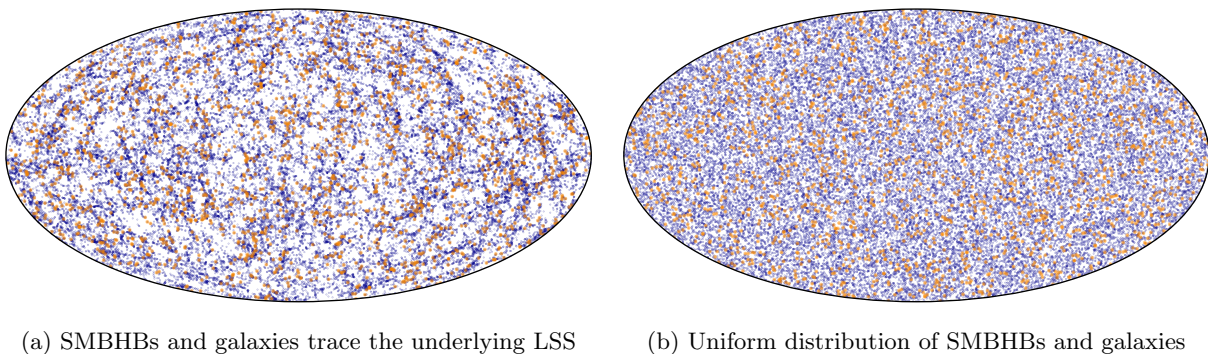


FIG. 1: SMBHBs are hosted by massive galaxies, which trace the LSS. Here we illustrate how a LSS-informed map (a) of galaxies (blue) and SMBHBs in these galaxies (orange) differ from one where the positions of both are isotropized (b). In this paper we show that LSS imprints spatial anisotropies in the GWB, even though only 1-4% of galaxies host SMBHBs [1]. This motivates our exploration of cross-correlations between galaxies and the GWB.

hide the LSS imprints in the GWB maps. This kind of loud-source anisotropy can be searched for and modeled using current techniques developed by e.g. [15, 20].

Targeting LSS-induced anisotropies and comparing them with galaxy clustering therefore provides a clear test of the nature of the GWB. Indeed, non-zero cross-correlations between the LSS and the GWB would support SMBHBs as the primary source of the GWB [21–24].

Here we explore the correlation between GWB anisotropies and galaxy clustering. Recently, [22, 23] investigated how cross-correlations can provide unique insights on the cosmic evolution of SMBHBs. They forecast the detectability of the cross-correlation between upcoming galaxy surveys and future PTA measurements of the GWB. While they employ a theoretical evaluation of the signals, we perform a rigorous simulation-based analysis to not only include the effect of the discreteness of the SMBHB population, but also to investigate the significance of the cross-correlation measurement in a single data realization. We do this by simulating the GWB, using a mock galaxy catalog combined with a semi-analytical model of the SMBHB population. We then develop a general framework that leverages cross-correlations with LSS to assess how distinguishable GWB and SMBHB population models are from each other. We focus on distinguishing a GWB informed by LSS, and one generated from a uniform distribution of SMBHBs. We explore the impact of cosmic variance for the first time in this kind of study, by comparing results from individual simulated realizations to those averaged over many simulations. Taking cosmic variance into account is crucial because neglecting it can lead to an error in estimating how detectable the LSS imprint is on the GWB.

The paper is organized as follows. In Section II, we describe the pipeline that is used to generate a mock galaxy distribution and GWBs. In Section III, we introduce the statistical formalism that allows to quantify the nature of the GWB anisotropies, while in Section IV we present the LSS-induced anisotropies detectability analysis. We discuss the impact of our results in Section V.

II. TRACERS OF LSS

Anisotropies in the spatial distribution of LSS tracers, such as galaxies and SMBHBs represent a biased tracer of the matter distribution, encoding information about their common evolution history. Here we consider the anisotropic distribution of galaxy number counts and the GWs emitted by SMBHBs. Briefly, we take a simulation-based approach, summarized in Figure 2. Starting from the ABACUSUMMIT suite of N -body simulations, we construct mock lightcones of galaxies by populating dark matter halos using the ABACUSHOD parametrization. We then populate these galaxies with SMBHBs using semi-analytical models from [8, 25]. From these galaxy and SMBHB catalogs, we build galaxy number count and GWB full-sky maps and study their angular statistics.

A. Galaxy distribution

To generate full-sky galaxy maps, we employ the ABACUSUMMIT suite of N -body simulations [26]. We use dark matter halo merger trees to construct the cosmic evolution across the radial direction, effectively building a halo lightcone. Specifically, we use one of the two *huge* simulations (box size of $7600 h^{-1}\text{Mpc}$ and 8640^3 particles of mass $M_{\text{part}} = 2.1 \times 5 \times 10^{10} h^{-1} M_{\odot}$). Observers are placed at the center of the box and can observe galaxies up to the half-distance of the box, $3.75 h^{-1}\text{Gpc}$.

The halo lightcone catalog is then populated with galaxies using the halo occupation distribution (HOD) model [27–29], which statistically connects the distribution of galaxies to their host dark matter haloes. We also include parameters to account for the dependence of each galaxy on its host halo mass, redshift, type, and environment, to better match current observations of galaxy clustering [30, 31]. We employ the ABACUSHOD prescription [32] to populate the haloes with luminous red galaxies (LRGs; see Appendix A for more details). We validated the statistical distribution of the simulated lightcone against the theoretical prediction from

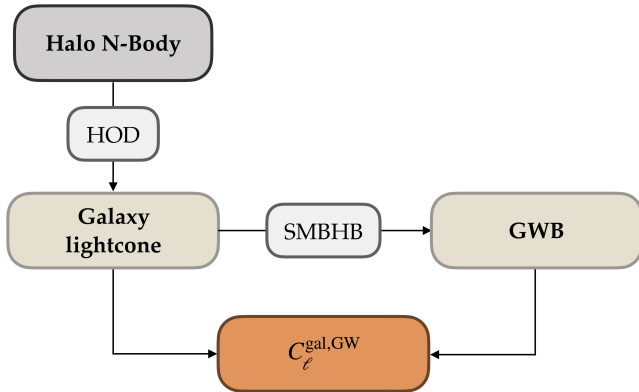


FIG. 2: Flow-chart of our pipeline. The galaxy lightcone is built from the ABACUSUMMIT suite of N -body simulations using the ABACUSHOD prescription. The SMBHB populations are created using a semi-analytical model from [8, 25], from which the GWB is computed. The galaxy distribution and the GWB are then cross-correlated to study the LSS imprint on the GWB.

CLASS [33]. For now we focus on the density term of the galaxy number count, and in the future we will include projection effects and redshift-space distortions.

To assign stellar masses to galaxies, we use the stellar mass (M_*) to halo mass (M_h) ratio from the UNIVERSEMACHINE framework [34]. The UNIVERSEMACHINE approach parameterizes the galaxy star formation rate as a function of the halo potential well depth, redshift, and assembly history. The redshift-dependent stellar-mass-to-halo-mass ratio fits are provided for both central and satellite galaxies. Due to simulation bounds, the distribution is truncated outside the range $z \in [0.1, 2]$. This limitation is particularly relevant for low redshifts, where the highest-strain GW sources are expected to be located. The exploration of the low-redshift regime is left for future work. Here we focus on a redshift range in which LSS anisotropies are expected to be significant, assuming that low-redshift sources will be detected as continuous GW signals. Appendix A provides details on the generation of mock galaxy catalogs.

B. The Gravitational wave background

Galaxies are populated by SMBHBs following the prescriptions in [8, 25, 37]. This accounts for galaxy total mass, bulge mass, merger fractions, merger timescales, and SMBH masses. We generate $N_r = 1,000$ SMBHB population realizations for the same galaxy distribution to account for cosmic variance. Each realization has a SMBHB population sampled from the differential number of SMBHBs per unit of total mass M , mass ratio q , redshift z , and frequency f_{GW} , defined as [37–39]:

$$\mathcal{N}_{\text{BHB}}(M, q, z, f_{\text{GW}}) = \frac{d^3 \Phi_{\text{BHB}}}{dM dq dz} \frac{dV}{df_r} \frac{dt_r}{df_{\text{GW}}}, \quad (1)$$

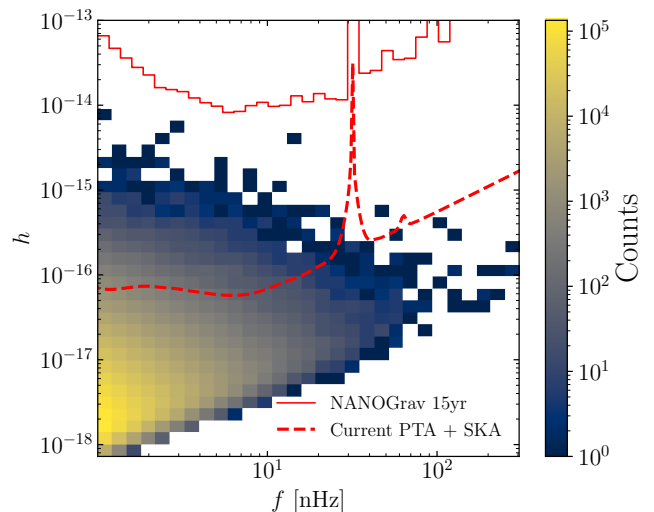


FIG. 3: Loud GW sources are present across all frequencies. While few in number, they contribute significantly to the GWB anisotropy. They must therefore be removed in order to find the LSS imprint in GWB. Here we show the frequency and strain distribution for one realization of the SMBHB population, with the detection curves for current and future PTA experiments from [35, 36].

where Φ_{BHB} is the comoving number density of SMBHB mergers, dV/dz is the comoving volume element [39], $f_r = f_{\text{GW}}(1+z)$ is the rest frame GW frequency, and t_r is the residence timescale [38]. The sky- and polarization-averaged strain emitted by each SMBHB is given by [6, 40, 41]

$$h = \frac{8}{\sqrt{10}} \frac{\mathcal{M}_o^{5/3} (\pi f_{\text{GW}})^{2/3}}{D_L(z)}, \quad (2)$$

where $D_L(z)$ is the luminosity distance, \mathcal{M} and $\mathcal{M}_o = \mathcal{M}(1+z)$ are the chirp masses in the source and observer frame, respectively. The characteristic strain of the GWB is typically parametrized as $h_c(f_{\text{GW}}) = A_{\text{yr}} (f_{\text{GW}}/f_{\text{yr}})^\alpha$, where A_{yr} is the GWB amplitude at a reference frequency $f_{\text{yr}} = 1 \text{ yr}^{-1}$ and $\alpha = -2/3$ is the spectral index for a GWB sourced by SMBHBs [6, 17]. Each GWB realization is consistent with the NANOGrav results, $A_{\text{yr}} = 2.4_{-0.6}^{+0.7} \times 10^{-15}$ [1, 25].

In Figure 3 we see the typical strain and frequency distribution of a SMBHB population realization, along with the sky-averaged sensitivity curve for resolvable SMBHBs for the NANOGrav 15 yr dataset [36, 42] and for future PTA experiments [35]. The NANOGrav 15 yr detection curve is based on the noise parameters in [43] and on the upper limits on the GW amplitude from individual binaries from [36]. The SKA sensitivity curve is computed as in [35], using the open-source Python package `hasasia` and the signal-to-noise estimates from [44]. We set a signal-to-noise of $S/N = 3$ on the GW strain, as typically assumed for detection of single sources in the nHz band. We draw PTA-suitable pulsars from the planned SKA MID and LOW survey distributions [45]. We in-

clude current NANOGrav pulsars, assuming that SKA PTA will be based on extended PTA datasets. We then add 4 pulsars per year with $\text{RMS} = 300 \pm 100$ ns, and cadences based on those in [35, 43].

C. Map-making and analysis

We build full sky maps of our tracers $X = \{\text{gal}, \text{GW}\}$ (where X is either the number count for galaxies or the characteristic strain for SMBHBs) and study the spatial anisotropies of their overdensity field, defined as [46]:

$$\delta^X(\hat{n}) = \frac{X(\hat{n})}{\bar{X}} - 1, \quad (3)$$

where \bar{X} is the field mean value and \hat{n} is the line-of-sight direction. For galaxies, we construct galaxy number count maps $N(z_i, \hat{n})$. For each redshift bin z_i , we count galaxies within each HEALPix-distributed pixel of a skymap [47, 48]. For the GWB, we construct a map of the characteristic strain as [41]:

$$h_c^2(f_{\text{GW}}, \hat{n}) = \frac{\sum_k h_k^2 f_{\text{GW},k}}{\Delta f_{\text{GW}}}, \quad (4)$$

where k runs over all the sources in a given frequency bin and direction, $\Delta f_{\text{GW}} = T_{\text{obs}}^{-1}$ is the frequency sampling interval, and T_{obs} is the total observation time. The information on clustering properties is enclosed in the n -point functions of the overdensity field. Since we are considering full-sky maps, it is more convenient to expand the overdensity field in spherical harmonics as

$$\delta^X(\hat{n}) = \sum_{\ell m} a_{\ell m}^X Y_{\ell m}(\hat{n}), \quad (5)$$

where $a_{\ell m}^X$ are the spherical harmonics coefficients and $Y_{\ell m}$ are spherical harmonics. The observed harmonic coefficients can be decomposed into a signal $s_{\ell m}^X$ and noise $n_{\ell m}^X$ component, so that $a_{\ell m}^X = s_{\ell m}^X + n_{\ell m}^X$. The total *theoretical* two-point function in harmonic space, i.e., the angular power spectrum \tilde{C}_ℓ , for any two tracers is then:

$$\langle a_{\ell m}^X a_{\ell' m'}^{Y*} \rangle = \delta_{\ell\ell'}^K \delta_{mm'}^K \tilde{C}_\ell^{XY}, \quad (6)$$

where δ^K is the Kronecker delta and $\langle \cdot \rangle$ denotes the ensemble average. Under the assumption that signal and noises are uncorrelated, i.e., $\langle s_{\ell m}^X n_{\ell' m'}^{Y*} \rangle = \langle n_{\ell m}^X n_{\ell' m'}^{Y*} \rangle = 0$, the total theoretical angular power spectrum is given by:

$$\tilde{C}_\ell^{XY} = C_\ell^{XY} + \delta_{XY}^K N_\ell^X, \quad (7)$$

where C_ℓ^{XY} is the clustering signal we are aiming to constrain, either $C_\ell^{\text{gal}, \text{gal}}$ [46, 49, 50], $C_\ell^{\text{GW}, \text{GW}}$ [15, 51] or the cross term $C_\ell^{\text{gal}, \text{GW}}$, and N_ℓ^X is angular power spectrum of tracer X shot noise. The *observed* angular power spectrum (the sum of the signal and noise) is:

$$\hat{C}_\ell^{XY} = \frac{1}{2\ell+1} \sum_{m=-\ell}^{\ell} a_{\ell m}^X (a_{\ell m}^Y)^*. \quad (8)$$

This angular power spectrum is computed from the product of two realizations of tracers X and Y . Since for each ℓ the number of $a_{\ell m}$ modes is finite, cosmic variance arises among realizations of the same underlying theory \tilde{C}_ℓ .

III. DISTINGUISHING ANISOTROPY MODELS

Previous cross-correlation studies have addressed the issue of distinguishing between different underlying scenarios (see e.g., [52–55]). In this work, we focus on a simulation-based approach, and introduce additional complexity into the analysis due to the stochastic nature of different realizations.

A. Intrinsic realization variances

The statistics of each individual stochastic realization never fully match the underlying theoretical model. Indeed, the measured angular power spectra \hat{C}_ℓ will be “scattered” around the theoretical value \tilde{C}_ℓ . First we aim to quantify such intrinsic (I) “scatter” for realizations of a given theory. A potential avenue involves defining a $\chi_{I,r}^2$ statistics for each realization r as

$$\chi_{I,r}^2 \equiv \sum_{\ell=2}^{\ell_{\text{max}}} \frac{2\ell+1}{2} \text{Tr} \left[\Delta \mathcal{C}_\ell \left(\mathcal{C}_\ell^{(\text{th})} \right)^{-1} \Delta \mathcal{C}_\ell \left(\mathcal{C}_\ell^{(\text{th})} \right)^{-1} \right], \quad (9)$$

where $\Delta \mathcal{C}_\ell = \mathcal{C}_\ell^{(r)} - \mathcal{C}_\ell^{(\text{th})}$; $\mathcal{C}_\ell^{(\text{th})}$ is an array containing the theoretical angular power spectra and $\mathcal{C}_\ell^{(r)}$ contains its measured value in a given realization. For each angular scale ℓ , given two galaxy redshift bins z_i, z_j and GWB frequency bins f_p, f_q , the \mathcal{C}_ℓ is arranged as [55, 56]:

$$\mathcal{C}_\ell = \begin{array}{cccc} \begin{array}{c} \text{C}_{\ell, z_i, z_i}^{\text{gal}, \text{gal}} \\ \text{C}_{\ell, z_i, z_j}^{\text{gal}, \text{gal}} \\ \text{C}_{\ell, z_i, f_p}^{\text{gal}, \text{GW}} \\ \text{C}_{\ell, z_i, f_q}^{\text{gal}, \text{GW}} \end{array} & \begin{array}{c} \text{C}_{\ell, z_i, z_j}^{\text{gal}, \text{gal}} \\ \text{C}_{\ell, z_j, z_j}^{\text{gal}, \text{gal}} \\ \text{C}_{\ell, z_j, f_p}^{\text{gal}, \text{GW}} \\ \text{C}_{\ell, z_j, f_q}^{\text{gal}, \text{GW}} \end{array} & \begin{array}{c} \text{C}_{\ell, z_i, f_p}^{\text{gal}, \text{GW}} \\ \text{C}_{\ell, z_j, f_p}^{\text{gal}, \text{GW}} \\ \text{C}_{\ell, f_p, f_p}^{\text{GW}, \text{GW}} \\ \text{C}_{\ell, f_p, f_q}^{\text{GW}, \text{GW}} \end{array} & \begin{array}{c} \text{C}_{\ell, z_i, f_q}^{\text{gal}, \text{GW}} \\ \text{C}_{\ell, z_j, f_q}^{\text{gal}, \text{GW}} \\ \text{C}_{\ell, f_p, f_q}^{\text{GW}, \text{GW}} \\ \text{C}_{\ell, f_q, f_q}^{\text{GW}, \text{GW}} \end{array} \end{array}$$

This form of the covariance allows to clearly visualize the relation between the observables, and can be extended to any number of frequency and redshift bins. The block-diagonal part includes correlations within the

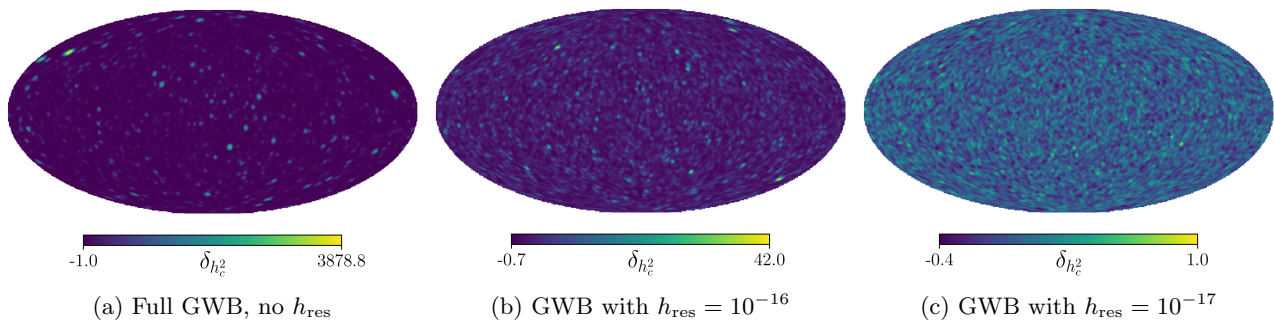


FIG. 4: Maps of the GWB characteristic strain overdensities, $\delta_{h_c^2}$. Large-strain sources appear as bright spots, making the C_ℓ indistinguishable from a uniform distribution of sources. Moving left to right, we progressively remove the “loudest” large-strain sources up to a cut h_{res} . By resolving them, anisotropies of the GWB generated by the remaining unresolved population are a representative sample of LSS anisotropies. While we use $h_{\text{res}} = 10^{-16}$ throughout this paper, here we show a $h_{\text{res}} = 10^{-17}$ map to highlight the potential of future PTA experiments to probe the LSS.

same tracer: the top-left block encodes the gal \times gal terms between all redshift bins (light blue), while the lower-right one encodes the GWB \times GWB terms between all frequency bins (green). The off-diagonal blocks encode the cross correlation gal \times GWB across different frequency and redshift bins. See Appendix B for an equivalent covariance matrix expression.

In our simulation-based approach, where we generate galaxy and SMBHBs populations, theoretical angular power spectra and covariance matrices are not known a priori, but have to be deduced from the suite of N_r realizations. We estimate the expectation value of the theoretical angular power spectra as

$$C_\ell^{(\text{th})} = \bar{C}_\ell = \frac{1}{N_r} \sum_{j=1}^{N_r} \hat{C}_{\ell,j}, \quad (10)$$

where the overbar denotes the average value across realizations. The average value and estimated variance of the $\chi_{I,r}^2$ for our suite of realizations are respectively defined as

$$\bar{\chi}_I^2 = \frac{1}{N_r} \sum_r \chi_{I,r}^2, \quad \sigma_{\chi_I^2}^2 = \frac{1}{N_r} \sum_r (\chi_{I,r}^2 - \bar{\chi}_I^2)^2. \quad (11)$$

If the angular power spectra were independent Gaussian random variables, the expected value for $\bar{\chi}_I^2$ and $\sigma_{\chi_I^2}^2$ could be derived theoretically and would be approximately proportional to the number of degrees of freedom of the system, i.e., to ℓ_{max} . However, when the random variables are correlated, as in the case at hand since in general $C_\ell^{\text{gal,GW}} \neq 0$, the expected value of the average chi-squared and its variance must also be deduced by producing a suite of realizations.

B. Comparing models

After quantifying the intrinsic variance of our realizations, we can estimate whether a realization from model A is statistically distinguishable from the average realization of a fiducial model B. We define for each realization

of model A a model comparison (MC) $\chi_{\text{MC},r}^2$ statistics, defined as

$$\chi_{\text{MC},r}^2 = \sum_{\ell=2}^{\ell_{\text{max}}} \frac{2\ell+1}{2} \times \text{Tr} \left[\Delta C_\ell \left(C_\ell^{(\text{th},\text{B})} \right)^{-1} \Delta C_\ell \left(C_\ell^{(\text{th},\text{B})} \right)^{-1} \right], \quad (12)$$

where $\Delta C_\ell = C_\ell^{(r,\text{A})} - C_\ell^{(\text{th},\text{B})}$, and where each quantity is computed as described in the previous Section. The value of this new chi-squared statistics is then compared to that of the previous section to assess, with a certain confidence level, whether the deviations from a theoretical model are not compatible with the effect of having different stochastic realizations of the same model. We then introduce a significance statistics D_r for model distinguishability for each realization r as

$$D_r = \frac{|\chi_{\text{MC},r}^2 - \bar{\chi}_I^2|}{\sigma_{\chi_I^2}}. \quad (13)$$

Here we consider a LSS-informed GWB as fiducial model, i.e., model B, and we aim to assess whether a uniform distribution of SMBHBs can be confidently ruled out as a possible interpretation of the observed signal. The statistics defined in equation 13 allows us to establish that if realization has $D_r > 1, 2, 3$ the uniform model can be excluded at 1, 2, 3 σ level.

IV. RESULTS

A. Loud sources and C_ℓ distributions

In Figure 1 we illustrate the SMBHB distribution follows the LSS, and that therefore GWB anisotropy can be LSS-induced. However, in the context of the GWB, every binary is effectively “weighted” by their GW strain, which in turn depend on the astrophysical parameters of the binaries. Therefore the statistics of GWB sky maps might be affected by this extra level of stochasticity on

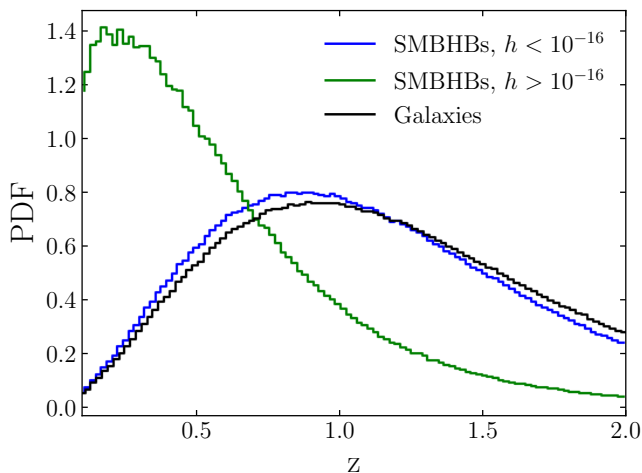


FIG. 5: Loud SMBHBs trace a different redshift distribution than the bulk of SMBHBs which source the GWB. Here we show galaxy and SMBHB redshift distributions, averaged over 1,000 realizations. Loud sources are concentrated at low redshifts, where they act as Poisson-like noise, resulting in anisotropies dominated by a small number of sources. The majority of unresolved SMBHBs creating the GWB spans a larger redshift that traces the underlying galaxy population. Since SMBHBs with $h < 10^{-16}$ (blue curve) are a subset of galaxies in our simulations, their distributions are very similar to Galaxies (black curve) but not identical.

top of the stochasticity of spatial distribution of sources we aim to constrain.

Figure 4 shows the anisotropic GWB sky map obtained from a single realization including all the sources with emitted strain below a threshold h_{res} . The threshold h_{res} is defined as the minimum strain for a source to be resolved. In particular, we observe that for large values of the threshold the anisotropies of the maps are totally dominated by the presence of “loud”, i.e., large strain, sources which appear as bright spots. These loud sources are also located in galaxies, most likely at low redshifts as showed in Figure 5, thus they still trace the LSS. However, since anisotropies are completely dominated by a very low number of binaries, their statistic is fundamentally indistinguishable from a uniform, Poisson-like distribution of SMBHBs point sources [15, 57, 58]. By resolving and characterizing individual SMBHBs, one may effectively remove their contribution from the unresolved population. In our simulations and fiducial SMBHB model, threshold values of $h_{\text{res}} = 10^{-14}, 10^{-15}, 10^{-16}$, correspond to an average number of resolved sources of around $\lesssim 1, 30, 3600$, respectively.

On the other hand, we observe that by lowering the sensitivity threshold and removing loud sources, we converge towards an actual background scenario, where the global GW emission is the incoherent superposition of many individual unresolved sources, see, e.g., right panel of Figure 4, and the statistics becomes more representative of the spatial distribution of galaxies hosting SMB-

HBs. Additionally, low strain sources trace a volume of the Universe similar to that probed by the bulk of galaxies, as also showed in Figure 5, therefore we expect them to be more correlated with LSS.

In terms of the statistical properties of GWB sky maps, we observe that when high strain sources are included, maps are effectively shot-noise dominated, and the stochasticity connected to astrophysics induces a large variance between different realizations. Conversely, removing loud sources we tend towards a situation where the bulk of GWB is effectively given by incoherent superposition of many events, the central limit theorem applies and different realizations present a degree of anisotropy driven mostly by clustering properties. These two scenarios are presented in the top panel of Figure 6, where we show the \hat{C}_ℓ of a set of GWB realizations for two thresholds, h_{res} . The variance is driven by the high realization dependence of the loudest sources, both in number and spatial position.

Regarding angular power spectra, it is well known [59, 60] that \hat{C}_ℓ measured from different Gaussian realizations, i.e., sets of $a_{\ell m}$ harmonic coefficients, of the same underlying theory are statistically distributed according to a Wishart probability distribution function (PDF) $W(2\ell + 1, \bar{C}_\ell)$, with $(2\ell + 1)$ degrees of freedom and scale given by the mean \bar{C}_ℓ . However, that is not the case when loud sources are included. We show in the top panel of Figure 6 the comparison between the estimated C_ℓ s distributions from our suite of realizations, applying different sensitivity cuts.

In the bottom panel of Figure 6, one can clearly see that a high threshold for detectability h_{res} implies a significant deviation with respect to the Wishart distribution. Moreover, we perform a Kolmogorov–Smirnov test [61] to establish at which threshold the overdensity field has a two-point statistics that is compatible with a Wishart. We find that for $h_{\text{res}} \gtrsim 2.3 \times 10^{-15}$, the \hat{C}_ℓ distribution is not consistent with a Wishart PDF within 3σ in the range of ℓ modes we consider. This implies that the two-point function alone is not sufficient to describe the statistics of the field. This is especially relevant at the current sensitivity level of PTA experiments, which do not currently resolve any single GW sources. Therefore, in the following sections, we will perform the statistical analysis only for sensitivity cuts below this GWB strain limit, where GWB maps are dominated by a continuous distribution of sources, for which our Gaussian formalism provides a good description of the statistics of the field.

B. GWB×LSS Cross-correlation

For the purpose of maximizing the LSS-induced anisotropies, we create a single redshift and frequency bin for galaxies and GWB, respectively, and we consider the case where $h_{\text{res}} = 10^{-16}$. We find comparable results when including multiple redshift bins, and discuss prospects of frequency tomography in Section V. For each realization we obtain the GWB two-point statistics pro-

duced by SMBHBs uniformly distributed on the sphere by creating sub-realizations where SMBHBs angular positions are drawn from a uniform pdf, and by averaging over this new set of C_ℓ s. The obtained angular power spectrum is consistent with a flat shot-noise spectrum. Finally, the analysis of Section III is performed both excluding and including the cross-correlation signal, i.e., by setting the signal to zero in the corresponding covariance matrix entries, to emphasize its constraining power.

We show in Figure 7 the D factor for the auto-correlation only and cross-correlation analysis as a function of the maximum resolution of the PTA experiment. In each panel we show the statistics of each realization (either directly or by drawing a band that encloses them) and the median of the distribution. Despite having removed loud sources, using only the information contained in GWB auto-correlation does not allow us to discriminate between different SMBHBs spatial distributions, as showed in the top-left panel of the Figure. However, when cross-correlations are included in the analysis, we can distinguish between the two scenario at more than one sigma confidence when $\ell_{\max} \gtrsim 20$ and $h_{\text{res}} = 10^{-16}$, i.e., in a SKA-like survey.

Loud sources are expected to be scattered throughout the entire frequency range, see Figure 3, and the contribution to the characteristic strain is higher for high frequency sources as in equation 4. In a single-bin scenario, we then focus on a narrower frequency range to remove the high-frequency tail of the distribution that creates large overdensities in the GWB maps. Specifically, we stack the information from the first two NANOGrav frequency bins up to 6 nHz. We also computed results for varying f_{\max} , and found that the D coefficient at $\ell_{\max} = 70$ decreases as $D_{10\text{nHz}} \simeq 0.86 D_{6\text{nHz}}$ and $D_{20\text{nHz}} \simeq 0.6 D_{6\text{nHz}}$ respectively.

Importantly, we find that the ability to distinguish between different SMBHB spatial distributions improves significantly with increasing ℓ_{\max} . We achieve 1, 2, 3, and 5σ significance for $\ell_{\max} \gtrsim 20, 30, 42, 72$, respectively. This demonstrates that higher angular resolutions in PTA experiments are critical for extracting anisotropies imprinted by LSS. Our results imply that a realization of the GWB can provide a clear imprint of LSS anisotropies, and a cross-correlation approach is crucial to extract this signal. This further highlights the importance of resolving continuous GW sources in the GWB, leaving the unresolved population as a fair sample of the underlying LSS, and a linear overdensity field description to be a suitable statistic for a cosmological anisotropy analysis.

V. SUMMARY AND DISCUSSION

Cross-correlation analysis between the GWB and LSS is a critical tool for unraveling the complex nature of the GWB. In this work we showed how the GWB generated by SMBHBs is an effective tracer of the LSS of our Universe. We produced 1,000 realizations of galaxy catalogs

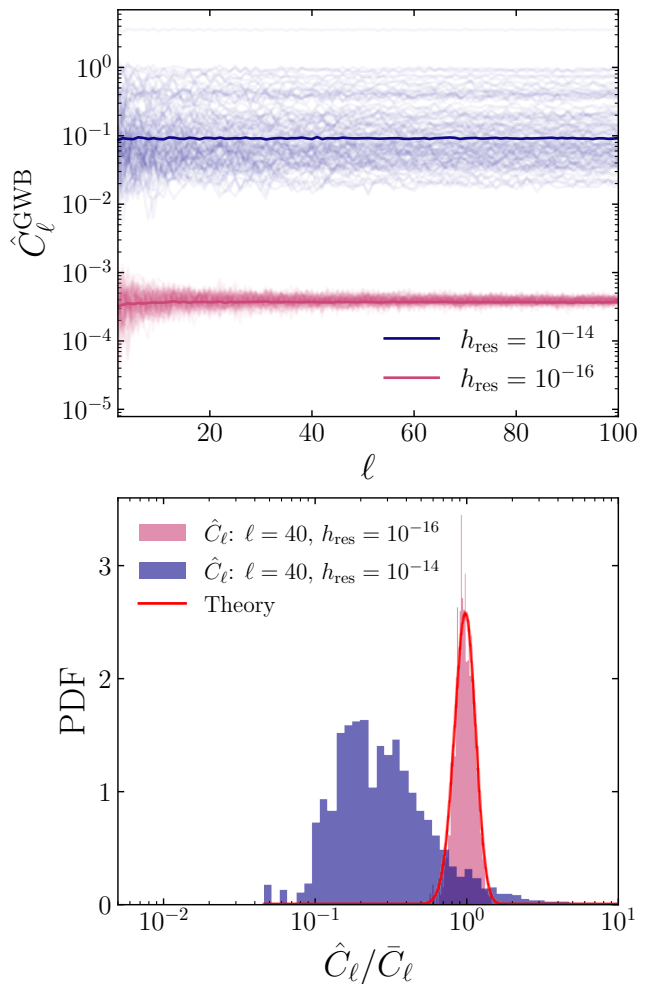


FIG. 6: *Top panel:* Angular power spectra \hat{C}_ℓ of 1,000 GWB realizations for two detection thresholds, h_{res} . The median C_ℓ value is the solid line. Even when the loudest GW sources are not resolved, they introduce a large variance in the \hat{C}_ℓ and the statistics are completely Poisson-noise dominated. As we lower the h_{res} threshold, the variance decreases and the scatter in the \hat{C}_ℓ distribution becomes more consistent with cosmic variance. *Bottom panel:* Distribution of the \hat{C}_ℓ for a fixed angular scale, compared to the expected Wishart distribution (both rescaled for visualization purposes). The scatter is consistent with the cosmic variance for $h_{\text{res}} \lesssim 2.3 \times 10^{-15}$, while for higher thresholds the distribution is not compatible with a Wishart distribution [59, 60] within 3σ .

and their subsequent and SMBHB catalogs directly from dark matter N -body simulations. We then built full-sky overdensity maps of galaxy number counts and GWB characteristic strain, without relying on a parametrized model of the angular power spectra, as was done by [22].

We investigated the impact of loud GW sources on the statistics of the GWB anisotropies, proving that for $h_{\text{res}} \gtrsim 10^{-15}$ the C_ℓ distribution is not compatible with a Wishart distribution within 3σ . This means that C_ℓ s are not the best suited summary statistic for the

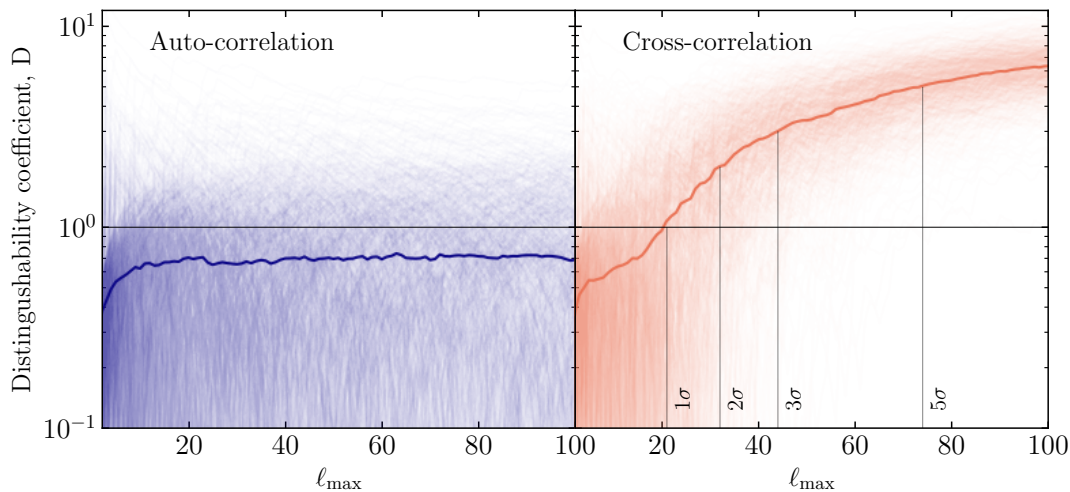


FIG. 7: LSS becomes measurable via cross-correlation searches in PTA experiments at a 1, 2, 3, 5 σ level ($D = 1, 2, 3, 5$) for $\ell_{\max} \geq 20, 30, 42, 72$, respectively, where D is the distinguishability coefficient. Each realization is plotted in light shade with a dark median. We assume a resolvability threshold of $h_{\text{res}} \geq 10^{-16}$ and a maximum frequency of $f_{\max} = 6$ nHz. *Left*: Using just the auto-correlation, LSS-induced anisotropies are indistinguishable from the ones sourced by a uniform distribution of sources. *Right*: A cross-correlation analysis provides $D \geq 1$ for $\ell_{\max} \gtrsim 20$.

GWB. Indeed, this is very relevant for current PTA experiments, since it implies that the central limit theorem does not apply to GWB maps, and the C_ℓ statistics therefore do not fully capture the information content and features of the GWB.

We also showed that using our method, given one realization of the GWB, such as the one we inhabit, we can robustly distinguish between a GWB with an imprint of the LSS and uniform distribution of SMBHBs at better than 3σ with a next-generation PTA experiment such as SKA [35]. This is achievable if sources with strain larger than $h_{\text{res}} \gtrsim 10^{-16}$ are resolved, which is feasible with the SKA [35]. The LSS imprint can be detected at 1σ , 2σ , 3σ , and 5σ significance levels for maximum angular resolutions of $\ell_{\max} = 20, 30, 42$, and 72 , respectively. Furthermore, our work shows that an approach based only on the GWB auto-correlation does not allow to distinguish between SMBHB distribution models, while a cross-correlation analysis does. Recently, [62, 63] also found that the Poisson noise contribution from a finite number of SMBHBs has a much larger impact on deviations from Hellings and Downs correlations [64] – used to detect an isotropic GWB – than anisotropies from the LSS.

While [65] explored how SMBHB clustering can trace the LSS, they did not carry out a cross-correlation analysis. Furthermore [22, 23] developed a theoretical formalism to forecast cross-correlation signals between the GWB and LSS, however their method cannot accurately predict the impact of the discreteness of the SMBHB population. We show that this is particularly relevant for the loudest low-redshift sources, with important implications on the GWB C_ℓ and the cross-correlation signal – that is to say that the C_ℓ s fail to capture the features of the GWB, as we explained above. While they employ the

theoretical ensemble-average estimate of the signal, we focus on a single realizations to provide intuition for future real-data analyses.

We now consider the accuracy and limitations of our methods. Here we consider galaxy clustering with a single redshift bins, however a tomographic approach might allow us to better capture the underlying properties of the population that sources the GWB. Such an approach would require the generation of more accurate lightcones which include both redshift-space distortions [66–68] and projection effects [69–73] to have an unbiased estimates of the cross-bin angular power spectra $C_{\ell, z_i, z_j}^{\text{gal, gal}}$ [74–79]. Moreover, by populating the lightcone with different kinds of galaxies we will be able to better understand the nature of the cross-frequency power spectra $C_{\ell, f_p, f_q}^{\text{GW, GW}}$. This will ultimately help us to design an optimal frequency binning strategy in such a cross-correlation search.

Our efforts here were focused on predicting what the GWB signal looks like in nature, and LSS imprints would ever be detectable, and if so, how to detect them. However, we did not simulate what this signal would look like in PTA data. In a future study, we plan to do this by adding pulsar noise [80, 81], accounting for the anisotropic distribution of pulsars on the sky [57, 82], as well as the way the GWB is detected [15, 64, 83]. All these improvements will help us to better model the expected signal in our cross-correlation searches, and improve our abilities to detect it.

We also plan to employ our general framework to test the connection between GWB anisotropies and the underlying SMBHB population properties, especially in light of the existence of low-redshift, loud sources located in the local Universe, whose existence appear to

be in disagreement with EM observations [14, 84]. Our new pipeline allows the construction of realistic GWBs directly from dark matter simulations, which can be implemented in a full Bayesian data analysis. This will in turn provide an avenue to directly constrain the physics driving the SMBHB mergers and, eventually, cosmological parameters themselves.

In summary, this work highlights the importance of cross-correlation techniques in characterizing and analyzing GWB, effectively making it another tracer of LSS. In fact, our technique can be used to explore the possible existence of a cosmological GWB component [9–13], in addition to an astrophysical one. Indeed, since cosmological GWB anisotropies share common statistical features with e.g. the Cosmic Microwave Background [85], it would be interesting to explore e.g. a 3×2 pt function cross-correlation analysis between the CMB, the LSS, and the GWB. As observational techniques continue to improve and more data becomes available, this novel framework will allow us to explore fundamental physics not accessible by any other means.

ACKNOWLEDGEMENTS

The authors would like to thank Bjorn Larsen, Eleonora Vanzan, Sarah Libanore, Sabino Matarrese, Nikhil Padmanabhan, and Deepali Agarwal for useful discussions and comments on the draft. This work is partly supported by ICSC - Centro Nazionale di Ricerca in High Performance Computing, Big Data and Quantum Computing, funded by European Union - NextGenerationEU. CMFM acknowledges support from the National Science Foundation from Grants NSF PHY-2020265 and AST-2414468. This work was also supported by the Flatiron Institute, part of the Simons Foundation. AR acknowledges funding from the Italian Ministry of University and Research (MIUR) through the “Dipartimenti di eccellenza” project “Science of the Universe”. NBe is supported by PRD/ARPE 2022 “Cosmology with Gravitational waves and Large Scale Structure - CosmoGraLSS”. DB acknowledges partial financial support from the COSMOS network (www.cosmosnet.it) through the ASI (Italian Space Agency) Grants 2016-24-H.0, 2016-24-H.1-2018 and 2020-9-HH.

Appendix A: Galaxy mock catalog

1. HOD

The baseline ABACUSHOD prescription [32] parametrizes the mean expected number of central and satellite galaxies per halo as a function of halo mass

with five parameters: $M_{\text{cut}}, M_{1-\text{sat}}, \sigma_M, \alpha_M, \kappa$ as

$$N_{\text{cent}}^{\text{LRG}}(M) = \frac{1}{2} \operatorname{erfc} \left[\frac{\log_{10}(M_{\text{cut}}/M)}{\sqrt{2}\sigma_M} \right], \quad (\text{A1})$$

$$N_{\text{sat}}^{\text{LRG}}(M) = \left[\frac{M - \kappa M_{\text{cut}}}{M_1} \right]^{\alpha_M} N_{\text{cent}}^{\text{LRG}}(M). \quad (\text{A2})$$

Here, M_{cut} and κM_{cut} encodes the minimum halo mass to host a central and satellite galaxy respectively. M_1 is the characteristic halo mass that hosts one satellite galaxy. α is the power law index on the number of satellite galaxies, while σ characterizes the transition tilt in the number of central galaxies. The model enforces each halo to host at most one central galaxy, which is placed on the center of mass of the largest sub-halo. The number of satellite galaxies is drawn from a Poisson distribution centered in $\bar{n}_{\text{sat}}^{\text{LRG}}(M)$, and they are assigned to particles within the halo with equal weights.

2. Stellar masses

To assign stellar masses to the galaxies, we use the stellar mass (M_*) to halo mass (M_h) ratio (SMHM ratio) from the UNIVERSEMACHINE approach [34], which provides a self-consistent fit to experimental data by connecting the star formation history to the properties of the host. The UNIVERSEMACHINE framework parametrizes the galaxy star formation rate as a function of the halo potential well depth, redshift, and assembly history. The SMHM fits are provided both for central and satellite galaxies, including redshift dependence (although redshift evolution is not significant for redshifts $z \lesssim 5$). The SMHM relation is parametrized as a double power-law plus a Gaussian function of the form

$$\log_{10} \left(\frac{M_*}{M_1} \right) = \epsilon - \log_{10} (10^{-\alpha x} + 10^{-\beta x}) + \gamma \exp \left[-0.5 \left(\frac{x}{\delta} \right)^2 \right], \quad (\text{A3})$$

where $x = \log_{10}(M_h/M_1)$, and the parameters $\epsilon, \alpha, \beta, \gamma, \delta$ are functions of redshift. They are modelled as a linear combination of a constant term, a linear term, and a logarithmic term, plus a redshift-dependent term:

$$\begin{aligned} \log_{10} \left(\frac{M_1}{M_{\odot}} \right) &= M_0 + M_a(a-1) - M_{\text{lna}} \ln(a) + M_z z \\ \epsilon &= \epsilon_0 + \epsilon_a(a-1) - \epsilon_{\text{lna}} \ln(a) + \epsilon_z z \\ \alpha &= \alpha_0 + \alpha_a(a-1) - \alpha_{\text{lna}} \ln(a) + \alpha_z z \\ \beta &= \beta_0 + \beta_a(a-1) + \beta_z z \\ \delta &= \delta_0 \\ \log_{10}(\gamma) &= \gamma_0 + \gamma_a(a-1) + \gamma_z z \end{aligned} \quad (\text{A4})$$

where $a = 1/(1+z)$ is the cosmological scale factor, and the parameters are provided in Table J1 of [34]. The stellar mass is then assigned to the galaxies by drawing from

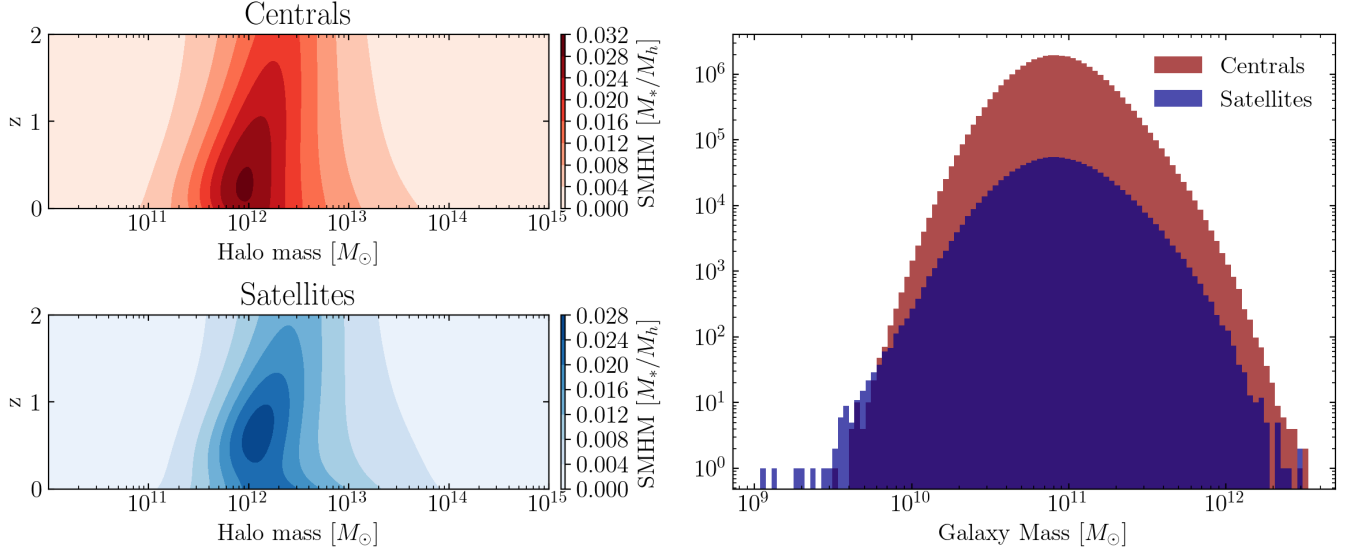


FIG. 8: *Left panel:* Stellar mass to halo mass relation for central and satellite galaxies for the redshift range considered in this work. *Right panel:* Galaxy mass histogram distribution for central and satellite galaxies.

the SMHM relation, also accounting for the scatter in the relation to introduce some stochasticity in the stellar mass assignment.

Figure 8 summarizes the mass-assignment prescription for both central and satellite galaxies. The left panel shows the SMHM relation as a function of halo mass and redshift, while the right panel shows the final mass distribution for the two sub-populations.

Appendix B: Statistics

1. Equivalent χ^2 formulation

The $\chi_{\text{MC},r}^2$ in equation (12) can be equivalently expressed as

$$\chi_{\text{MC},r}^2 = f_{\text{sky}} \sum_2^{\ell_{\text{max}}} (\Delta \Sigma_\ell)^T \mathcal{M}_\ell^{-1} (\Delta \Sigma_\ell), \quad (\text{B1})$$

where now $\Delta \Sigma_\ell = \mathbf{C}_\ell^{(r,A)} - \mathbf{C}_\ell^{(\text{th},B)}$. The quantity \mathbf{C}_ℓ encodes the data in \mathcal{C}_ℓ in a 1D vector as

$$\mathbf{C}_\ell = \begin{pmatrix} C_\ell^{\text{gal,gal}}(z_1, z_1) \\ \vdots \\ C_\ell^{\text{gal,GW}}(z_1, f_1) \\ \vdots \\ C_\ell^{\text{GW,GW}}(f_1, f_1) \\ \vdots \end{pmatrix}. \quad (\text{B2})$$

Due to the symmetry of \mathcal{C}_ℓ , only the diagonal and upper-diagonal entries are included. In order to be properly combined with the data vector of equation (B2), the new

covariance matrix \mathcal{M}_ℓ is constructed by associating to every index I and J of the column vector \mathbf{C}_ℓ a couple of indices (I_1, I_2) and (J_1, J_2) , to encode the two tracers in a given redshift or frequency (e.g., for $C_\ell^{\text{gal,GW}}(z_1, f_1)$, $I_1 = \text{gal}_{z_1}$ and $I_2 = \text{GW}_{f_1}$). The new covariance matrix is then defined as

$$\mathcal{M}_\ell^{IJ} = \frac{1}{2\ell + 1} \left(C_\ell^{(I_1, J_1)} C_\ell^{(I_2, J_2)} + C_\ell^{(I_1, J_2)} C_\ell^{(I_2, J_1)} \right). \quad (\text{B3})$$

In practice, in a simulation-based analysis, the covariance matrix is computed by averaging over a set of M realizations, so that [53, 86]

$$\begin{aligned} \text{Cov} \left(C_\ell^{I_1 I_2}, C_\ell^{J_1 J_2} \right) &= \\ &= \frac{1}{M} \sum_{k=1}^M \left[\hat{C}_{\ell,k}^{I_1 I_2} - \bar{C}_\ell^{I_1 I_2} \right] \left[\hat{C}_{\ell,k}^{J_1 J_2} - \bar{C}_\ell^{J_1 J_2} \right], \quad (\text{B4}) \end{aligned}$$

where the bar denotes the ensemble average and the hat denotes the realization-dependent quantity. We validate the covariance matrix by comparing the ensemble average of the cross-correlation coefficients with the theoretical prediction of equation (B3).

2. χ^2 from simulations

In Figure 9, we illustrate the intrinsic $\chi_{I,r}^2$ and model-comparison $\chi_{\text{MC},r}^2$ distribution for all our realizations. These distributions are used to compute the D coefficients shown in Figure 7. We highlight the median of each quantity, and the shaded region represents the full bounds of the distribution across realizations. The $\chi_{I,r}^2$ coefficient quantifies how much a realization from a model

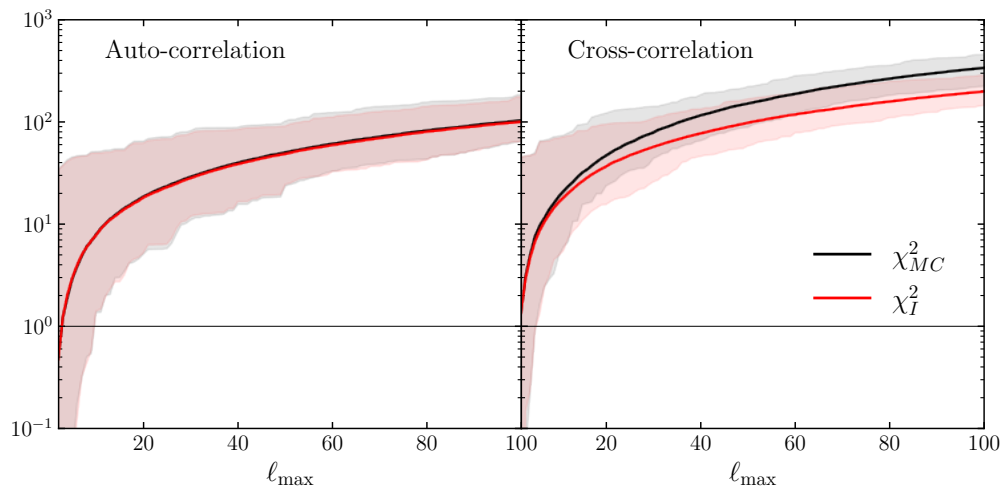


FIG. 9: Cross-correlations enable us to do model comparison. Here we show distributions of intrinsic $\chi_{I,r}^2$ and model-comparison $\chi_{MC,r}^2$ for all realizations. Shaded regions show the full distribution bounds, with medians highlighted. These distributions are used to compute the D coefficients in Figure 7. *Left panel:* The auto-correlation case shows overlapping distributions, indicating no significance when comparing a realization to a fiducial model. *Right panel:* In the cross-correlation setting, $\chi_{MC,r}^2$ exceeds $\chi_{I,r}^2$ when cross-correlations and small angular scales are included, enabling significant model comparison.

is statistically distinguishable from the average realization of a fiducial model. This is compared with the intrinsic scatter for realizations of a given theory (encoded in $\chi_{I,r}^2$) to build up the D statistics from equation 13.

In the left panel, the two distributions are fully compatible, hence we cannot distinguish a realization of the

fiducial model and one from a different model.

On the other hand, when including cross-correlations and sufficiently small angular scales, $\chi_{MC,r}^2$ is consistently above the $\chi_{I,r}^2$ distribution, implying that the model comparison can be carried out at high significance.

-
- [1] G. Agazie *et al.* (NANOGrav), The NANOGrav 15 yr Data Set: Evidence for a Gravitational-wave Background, *Astrophys. J. Lett.* **951**, L8 (2023), arXiv:2306.16213 [astro-ph.HE].
- [2] J. Antoniadis *et al.* (EPTA, InPTA:), The second data release from the European Pulsar Timing Array - III. Search for gravitational wave signals, *Astron. Astrophys.* **678**, A50 (2023), arXiv:2306.16214 [astro-ph.HE].
- [3] D. J. Reardon *et al.*, Search for an Isotropic Gravitational-wave Background with the Parkes Pulsar Timing Array, *Astrophys. J. Lett.* **951**, L6 (2023), arXiv:2306.16215 [astro-ph.HE].
- [4] H. Xu *et al.*, Searching for the Nano-Hertz Stochastic Gravitational Wave Background with the Chinese Pulsar Timing Array Data Release I, *Res. Astron. Astrophys.* **23**, 075024 (2023), arXiv:2306.16216 [astro-ph.HE].
- [5] R. S. Foster and D. C. Backer, Constructing a Pulsar Timing Array, *Astrophys. J.* **361**, 300 (1990).
- [6] A. Sesana, A. Vecchio, and C. N. Colacino, The stochastic gravitational-wave background from massive black hole binary systems: implications for observations with Pulsar Timing Arrays, *Mon. Not. Roy. Astron. Soc.* **390**, 192 (2008), arXiv:0804.4476 [astro-ph].
- [7] B. Bécsy, N. J. Cornish, and L. Z. Kelley, Exploring Realistic Nanohertz Gravitational-wave Backgrounds, *Astrophys. J.* **941**, 119 (2022), arXiv:2207.01607 [astro-ph.HE].
- [8] G. Agazie *et al.*, The NANOGrav 15 yr Data Set: Looking for Signs of Discreteness in the Gravitational-wave Background, (2024), arXiv:2404.07020 [astro-ph.HE].
- [9] V. Alba and J. Maldacena, Primordial gravity wave background anisotropies, *JHEP* **03**, 115, arXiv:1512.01531 [hep-th].
- [10] C. R. Contaldi, Anisotropies of Gravitational Wave Backgrounds: A Line Of Sight Approach, *Phys. Lett. B* **771**, 9 (2017), arXiv:1609.08168 [astro-ph.CO].
- [11] N. Bartolo, D. Bertacca, S. Matarrese, M. Peloso, A. Ricciardone, A. Riotto, and G. Tasinato, Characterizing the cosmological gravitational wave background: Anisotropies and non-Gaussianity, *Phys. Rev. D* **102**, 023527 (2020), arXiv:1912.09433 [astro-ph.CO].
- [12] L. Valbusa Dall'Armi, A. Ricciardone, N. Bartolo, D. Bertacca, and S. Matarrese, Imprint of relativistic particles on the anisotropies of the stochastic gravitational-wave background, *Phys. Rev. D* **103**, 023522 (2021), arXiv:2007.01215 [astro-ph.CO].
- [13] A. Afzal *et al.* (NANOGrav), The NANOGrav 15 yr Data Set: Search for Signals from New Physics, *Astrophys. J. Lett.* **951**, L11 (2023), arXiv:2306.16219 [astro-ph.HE].
- [14] G. Sato-Polito, M. Zaldarriaga, and E. Quataert, Where are the supermassive black holes measured by PTAs?, *Phys. Rev. D* **110**, 063020 (2024), arXiv:2312.06756

- [astro-ph.CO].
- [15] C. M. F. Mingarelli, T. Sidery, I. Mandel, and A. Vecchio, Characterizing gravitational wave stochastic background anisotropy with pulsar timing arrays, *Phys. Rev. D* **88**, 062005 (2013), arXiv:1306.5394 [astro-ph.HE].
- [16] G. Agazie *et al.* (NANOGrav), The NANOGrav 15 yr Data Set: Search for Anisotropy in the Gravitational-wave Background, *Astrophys. J. Lett.* **956**, L3 (2023), arXiv:2306.16221 [astro-ph.HE].
- [17] E. S. Phinney, A Practical theorem on gravitational wave backgrounds, (2001), arXiv:astro-ph/0108028.
- [18] M. C. Begelman, R. D. Blandford, and M. J. Rees, Massive black hole binaries in active galactic nuclei, *Nature* **287**, 307 (1980).
- [19] J. Kormendy and D. Richstone, Inward bound: The Search for supermassive black holes in galactic nuclei, *Ann. Rev. Astron. Astrophys.* **33**, 581 (1995).
- [20] S. R. Taylor, R. van Haasteren, and A. Sesana, From Bright Binaries To Bumpy Backgrounds: Mapping Realistic Gravitational Wave Skies With Pulsar-Timing Arrays, *Phys. Rev. D* **102**, 084039 (2020), arXiv:2006.04810 [astro-ph.IM].
- [21] C. M. F. Mingarelli, T. J. W. Lazio, A. Sesana, J. E. Greene, J. A. Ellis, C.-P. Ma, S. Croft, S. Burke-Spolaor, and S. R. Taylor, The Local Nanohertz Gravitational-Wave Landscape From Supermassive Black Hole Binaries, *Nature Astron.* **1**, 886 (2017), arXiv:1708.03491 [astro-ph.GA].
- [22] M. R. Sah and S. Mukherjee, Discovering the Cosmic Evolution of Supermassive Black Holes using Nanohertz Gravitational Waves and Galaxy Surveys, (2024), arXiv:2407.11669 [astro-ph.CO].
- [23] M. R. Sah, S. Mukherjee, V. Saeedzadeh, A. Babul, M. Tremmel, and T. R. Quinn, Imprints of supermassive black hole evolution on the spectral and spatial anisotropy of nano-hertz stochastic gravitational-wave background, *Mon. Not. Roy. Astron. Soc.* **533**, 1568 (2024), arXiv:2404.14508 [astro-ph.CO].
- [24] A.-M. Lemke, A. Mitridate, and K. A. Gersbach, Detecting Gravitational Wave Anisotropies from Supermassive Black Hole Binaries, (2024), arXiv:2407.08705 [astro-ph.HE].
- [25] J. A. Casey-Clyde, C. M. F. Mingarelli, J. E. Greene, K. Pardo, M. Nañez, and A. D. Goulding, A Quasar-based Supermassive Black Hole Binary Population Model: Implications for the Gravitational Wave Background, *Astrophys. J.* **924**, 93 (2022), arXiv:2107.11390 [astro-ph.HE].
- [26] B. Hadzhiyska, L. H. Garrison, D. Eisenstein, and S. Bose, The halo light-cone catalogues of AbacusSummit, *Mon. Not. Roy. Astron. Soc.* **509**, 2194 (2021), arXiv:2110.11413 [astro-ph.CO].
- [27] J. A. Peacock and R. E. Smith, Halo occupation numbers and galaxy bias, *Mon. Not. Roy. Astron. Soc.* **318**, 1144 (2000), arXiv:astro-ph/0005010.
- [28] R. Scoccimarro, R. K. Sheth, L. Hui, and B. Jain, How many galaxies fit in a halo? Constraints on galaxy formation efficiency from spatial clustering, *Astrophys. J.* **546**, 20 (2001), arXiv:astro-ph/0006319.
- [29] Z. Zheng, A. A. Berlind, D. H. Weinberg, A. J. Benson, C. M. Baugh, S. Cole, R. Dave, C. S. Frenk, N. Katz, and C. G. Lacey, Theoretical models of the halo occupation distribution: Separating central and satellite galaxies, *Astrophys. J.* **633**, 791 (2005), arXiv:astro-ph/0408564.
- [30] S. D. M. White and M. J. Rees, Core condensation in heavy halos: A Two stage theory for galaxy formation and clusters, *Mon. Not. Roy. Astron. Soc.* **183**, 341 (1978).
- [31] G. R. Blumenthal, S. M. Faber, J. R. Primack, and M. J. Rees, Formation of Galaxies and Large Scale Structure with Cold Dark Matter, *Nature* **311**, 517 (1984).
- [32] S. Yuan, L. H. Garrison, B. Hadzhiyska, S. Bose, and D. J. Eisenstein, AbacusHOD: a highly efficient extended multitracer HOD framework and its application to BOSS and eBOSS data, *Mon. Not. Roy. Astron. Soc.* **510**, 3301 (2022), arXiv:2110.11412 [astro-ph.CO].
- [33] J. Lesgourgues, The Cosmic Linear Anisotropy Solving System (CLASS) I: Overview, (2011), arXiv:1104.2932 [astro-ph.IM].
- [34] P. Behroozi, R. H. Wechsler, A. P. Hearin, and C. Conroy, UniverseMachine: The correlation between galaxy growth and dark matter halo assembly from $z = 0-10$, *Mon. Not. Roy. Astron. Soc.* **488**, 3143 (2019), arXiv:1806.07893.
- [35] C. Xin, C. M. F. Mingarelli, and J. S. Hazboun, Multimessenger Pulsar Timing Array Constraints on Supermassive Black Hole Binaries Traced by Periodic Light Curves, *Astrophys. J.* **915**, 97 (2021), arXiv:2009.11865 [astro-ph.GA].
- [36] G. Agazie *et al.* (NANOGrav), The NANOGrav 15 yr Data Set: Bayesian Limits on Gravitational Waves from Individual Supermassive Black Hole Binaries, *Astrophys. J. Lett.* **951**, L50 (2023), arXiv:2306.16222 [astro-ph.HE].
- [37] S. Chen, A. Sesana, and C. J. Conselice, Constraining astrophysical observables of Galaxy and Supermassive Black Hole Binary Mergers using Pulsar Timing Arrays, *Mon. Not. Roy. Astron. Soc.* **488**, 401 (2019), arXiv:1810.04184 [astro-ph.GA].
- [38] P. C. Peters and J. Mathews, Gravitational radiation from point masses in a Keplerian orbit, *Phys. Rev.* **131**, 435 (1963).
- [39] D. W. Hogg, Distance measures in cosmology, (1999), arXiv:astro-ph/9905116.
- [40] K. S. Thorne, Gravitational radiation, in *17th Texas Symposium on Relativistic Astrophysics* (1994) pp. 127–152.
- [41] P. A. Rosado, A. Sesana, and J. Gair, Expected properties of the first gravitational wave signal detected with pulsar timing arrays, *Mon. Not. Roy. Astron. Soc.* **451**, 2417 (2015), arXiv:1503.04803 [astro-ph.HE].
- [42] G. Agazie *et al.* (NANOGrav), The NANOGrav 15 yr Data Set: Detector Characterization and Noise Budget, *Astrophys. J. Lett.* **951**, L10 (2023), arXiv:2306.16218 [astro-ph.HE].
- [43] G. Agazie *et al.* (NANOGrav), The NANOGrav 15 yr Data Set: Constraints on Supermassive Black Hole Binaries from the Gravitational-wave Background, *Astrophys. J. Lett.* **952**, L37 (2023), arXiv:2306.16220 [astro-ph.HE].
- [44] J. S. Hazboun, J. D. Romano, and T. L. Smith, Realistic sensitivity curves for pulsar timing arrays, *Phys. Rev. D* **100**, 104028 (2019), arXiv:1907.04341 [gr-qc].
- [45] E. F. Keane *et al.*, A Cosmic Census of Radio Pulsars with the SKA, *PoS AASKA14*, 040 (2015), arXiv:1501.00056 [astro-ph.IM].
- [46] V. Springel, C. S. Frenk, and S. D. M. White, The large-scale structure of the Universe, *Nature* **440**, 1137 (2006), arXiv:astro-ph/0604561.
- [47] K. M. Górski, E. Hivon, A. J. Banday, B. D. Wandelt,

- F. K. Hansen, M. Reinecke, and M. Bartelman, HEALPix - A Framework for high resolution discretization, and fast analysis of data distributed on the sphere, *Astrophys. J.* **622**, 759 (2005), arXiv:astro-ph/0409513.
- [48] A. Zonca, L. Singer, D. Lenz, M. Reinecke, C. Rosset, E. Hivon, and K. Gorski, healpy: equal area pixelization and spherical harmonics transforms for data on the sphere in Python, *Journal of Open Source Software* **4**, 1298 (2019).
- [49] S. D. Landy and A. S. Szalay, Bias and variance of angular correlation functions, *Astrophys. J.* **412**, 64 (1993).
- [50] A. J. S. Hamilton, Toward Better Ways to Measure the Galaxy Correlation Function, *Astrophys. J.* **417**, 19 (1993).
- [51] N. Bartolo, D. Bertacca, S. Matarrese, M. Peloso, A. Ricciardone, A. Riotta, and G. Tasinato, Anisotropies and non-Gaussianity of the Cosmological Gravitational Wave Background, *Phys. Rev. D* **100**, 121501 (2019), arXiv:1908.00527 [astro-ph.CO].
- [52] A. Raccanelli *et al.*, Cosmological Measurements with Forthcoming Radio Continuum Surveys, *Mon. Not. Roy. Astron. Soc.* **424**, 801 (2012), arXiv:1108.0930 [astro-ph.CO].
- [53] T. Giannantonio, R. Scranton, R. G. Crittenden, R. C. Nichol, S. P. Boughn, A. D. Myers, and G. T. Richards, Combined analysis of the integrated Sachs-Wolfe effect and cosmological implications, *Phys. Rev. D* **77**, 123520 (2008), arXiv:0801.4380 [astro-ph].
- [54] A. Raccanelli, E. D. Kovetz, S. Bird, I. Cholis, and J. B. Munoz, Determining the progenitors of merging black-hole binaries, *Phys. Rev. D* **94**, 023516 (2016), arXiv:1605.01405 [astro-ph.CO].
- [55] G. Scelfo, N. Bellomo, A. Raccanelli, S. Matarrese, and L. Verde, GW \times LSS: chasing the progenitors of merging binary black holes, *JCAP* **09**, 039, arXiv:1809.03528 [astro-ph.CO].
- [56] N. Bellomo, J. L. Bernal, G. Scelfo, A. Raccanelli, and L. Verde, Beware of commonly used approximations. Part I. Errors in forecasts, *JCAP* **10**, 016, arXiv:2005.10384 [astro-ph.CO].
- [57] Y. Ali-Haïmoud, T. L. Smith, and C. M. F. Mingarelli, Insights into searches for anisotropies in the nanohertz gravitational-wave background, *Phys. Rev. D* **103**, 042009 (2021), arXiv:2010.13958 [gr-qc].
- [58] T. Konstandin, A.-M. Lemke, A. Mitridate, and E. Perboni, The impact of cosmic variance on PTAs anisotropy searches, (2024), arXiv:2408.07741 [astro-ph.CO].
- [59] S. Hamimeche and A. Lewis, Likelihood Analysis of CMB Temperature and Polarization Power Spectra, *Phys. Rev. D* **77**, 103013 (2008), arXiv:0801.0554 [astro-ph].
- [60] N. Bellomo, J. L. Bernal, G. Scelfo, A. Raccanelli, and L. Verde, Beware of commonly used approximations. Part I. Errors in forecasts, *JCAP* **10**, 016, arXiv:2005.10384 [astro-ph.CO].
- [61] N. Smirnov, Table for Estimating the Goodness of Fit of Empirical Distributions, *The Annals of Mathematical Statistics* **19**, 279 (1948).
- [62] N. Grimm, M. Pijenburg, G. Cusin, and C. Bonvin, The impact of large-scale galaxy clustering on the variance of the Hellings-Downs correlation, (2024), arXiv:2404.05670 [astro-ph.CO].
- [63] B. Allen, D. Agarwal, J. D. Romano, and S. Valtolina, Source anisotropies and pulsar timing arrays, (2024), arXiv:2406.16031 [gr-qc].
- [64] R. w. Hellings and G. s. Downs, UPPER LIMITS ON THE ISOTROPIC GRAVITATIONAL RADIATION BACKGROUND FROM PULSAR TIMING ANALYSIS, *Astrophys. J. Lett.* **265**, L39 (1983).
- [65] Q. Yang, X. Guo, Z. Cao, X. Shao, and X. Yuan, Anisotropy of Nanohertz Gravitational Wave Background and Individual Sources from Supermassive Binary Black Holes: Probe of Cosmic Large Scale Structure, (2024), arXiv:2408.05043 [astro-ph.CO].
- [66] N. Kaiser, Clustering in real space and in redshift space, *Mon. Not. Roy. Astron. Soc.* **227**, 1 (1987).
- [67] A. J. S. Hamilton, Linear redshift distortions: A Review, in *Ringberg Workshop on Large Scale Structure* (1997) arXiv:astro-ph/9708102.
- [68] A. Raccanelli, D. Bertacca, D. Pietrobon, F. Schmidt, L. Samushia, N. Bartolo, O. Dore, S. Matarrese, and W. J. Percival, Testing Gravity Using Large-Scale Redshift-Space Distortions, *Mon. Not. Roy. Astron. Soc.* **436**, 89 (2013), arXiv:1207.0500 [astro-ph.CO].
- [69] C. Bonvin and R. Durrer, What galaxy surveys really measure, *Phys. Rev. D* **84**, 063505 (2011), arXiv:1105.5280 [astro-ph.CO].
- [70] D. Jeong, F. Schmidt, and C. M. Hirata, Large-scale clustering of galaxies in general relativity, *Phys. Rev. D* **85**, 023504 (2012), arXiv:1107.5427 [astro-ph.CO].
- [71] A. Challinor and A. Lewis, The linear power spectrum of observed source number counts, *Phys. Rev. D* **84**, 043516 (2011), arXiv:1105.5292 [astro-ph.CO].
- [72] D. Bertacca, R. Maartens, A. Raccanelli, and C. Clarkson, Beyond the plane-parallel and Newtonian approach: Wide-angle redshift distortions and convergence in general relativity, *JCAP* **10**, 025, arXiv:1205.5221 [astro-ph.CO].
- [73] D. Bertacca, A. Raccanelli, N. Bartolo, M. Liguori, S. Matarrese, and L. Verde, Relativistic wide-angle galaxy bispectrum on the light-cone, *Phys. Rev. D* **97**, 023531 (2018), arXiv:1705.09306 [astro-ph.CO].
- [74] T. Matsubara, Y. Suto, and I. Szapudi, Light cone effect on higher order clustering in redshift surveys, *Astrophys. J. Lett.* **491**, L1 (1997), arXiv:astro-ph/9708121.
- [75] J. Yoo, A. L. Fitzpatrick, and M. Zaldarriaga, A New Perspective on Galaxy Clustering as a Cosmological Probe: General Relativistic Effects, *Phys. Rev. D* **80**, 083514 (2009), arXiv:0907.0707 [astro-ph.CO].
- [76] A. Raccanelli, D. Bertacca, D. Jeong, M. C. Neyrinck, and A. S. Szalay, Doppler term in the galaxy two-point correlation function: wide-angle, velocity, Doppler lensing and cosmic acceleration effects, *Phys. Dark Univ.* **19**, 109 (2018), arXiv:1602.03186 [astro-ph.CO].
- [77] E. Di Dio, F. Montanari, A. Raccanelli, R. Durrer, M. Kamionkowski, and J. Lesgourgues, Curvature constraints from Large Scale Structure, *JCAP* **06**, 013, arXiv:1603.09073 [astro-ph.CO].
- [78] F. Semenzato, D. Bertacca, and A. Raccanelli, The full-sky Spherical Fourier-Bessel power spectrum in general relativity, (2024), arXiv:2406.09545 [astro-ph.CO].
- [79] F. Spezzati and A. Raccanelli, 3D-Radial galaxy correlation function, (2024), arXiv:2408.01495 [astro-ph.CO].
- [80] G. Agazie *et al.* (NANOGrav), The NANOGrav 15 yr Data Set: Observations and Timing of 68 Millisecond Pulsars, *Astrophys. J. Lett.* **951**, L9 (2023), arXiv:2306.16217 [astro-ph.HE].
- [81] B. Larsen *et al.*, The NANOGrav 15 yr Data Set: Chromatic Gaussian Process Noise Models for Six Pulsars,

- Astrophys. J. **972**, 49 (2024), arXiv:2405.14941 [astro-ph.HE].
- [82] Y. Ali-Haïmoud, T. L. Smith, and C. M. F. Mingarelli, Fisher formalism for anisotropic gravitational-wave background searches with pulsar timing arrays, Phys. Rev. D **102**, 122005 (2020), arXiv:2006.14570 [gr-qc].
- [83] N. J. Cornish and R. van Haasteren, Mapping the nanohertz gravitational wave sky, (2014), arXiv:1406.4511 [gr-qc].
- [84] G. Sato-Polito and M. Zaldarriaga, The distribution of the gravitational-wave background from supermassive black holes, (2024), arXiv:2406.17010 [astro-ph.CO].
- [85] A. Ricciardone, L. V. Dall'Armi, N. Bartolo, D. Bertacca, M. Liguori, and S. Matarrese, Cross-Correlating Astrophysical and Cosmological Gravitational Wave Backgrounds with the Cosmic Microwave Background, Phys. Rev. Lett. **127**, 271301 (2021), arXiv:2106.02591 [astro-ph.CO].
- [86] S. Ho, C. Hirata, N. Padmanabhan, U. Seljak, and N. Bahcall, Correlation of CMB with large-scale structure: I. ISW Tomography and Cosmological Implications, Phys. Rev. D **78**, 043519 (2008), arXiv:0801.0642 [astro-ph].